Check for updates

Structure and performance of a V₂O₅–WO₃/TiO₂–SiO₂ catalyst derived from blast furnace slag (BFS) for DeNOₓ†

Tuyet-Suong Tran,[ab] Jian Yu,*[a] Changming Li,[a] Feng Guo,[a] Yusheng Zhang[a] and Guangwen Xu [ID] *[a]

The titanium-bearing blast furnace slag (BFS), a solid waste with high TiO_2 content (around 20%) and huge production (3.6 million tons per year), has caused serious environmental problems in China. The reuse of BFS in making DeNO$_x$ catalysts has been confirmed to be promising because of its low cost and high effectiveness for DeNO$_x$. In this work, four V_2O_5–WO_3/TiO_2–SiO_2 samples from BFS and commercial Ti/Si were made with different amounts of Al_2O_3/Fe_2O_3/SO_4^{2-} dopants to reveal the unique structure effect of a slag-based catalyst on the catalytic behavior for DeNO$_x$. Catalyst characterization clarified that the Al_2O_3/Fe_2O_3/SO_4^{2-} dopants from BFS may facilitate the formation of Ti–O–Si linkages with abundant structure defects. The structure possibly played a key role in acquiring a high surface area, well-dispersed active VO$_x$ species, sufficient weak acid sites and a high amount of O$_{ads}$ and V^{4+} species for the slag-based catalyst. These advantages in structure were confirmed by catalytic tests showing superior DeNO$_x$ performances. Nonetheless, too many SO_4^{2-} dopants caused agglomeration of TiO_2–SiO_2 particles, formation of strong acid sites and a high amount of O$_{ads}$ species to negatively impact the DeNO$_x$ activity, selectivity and catalyst lifetime.

1. Introduction

The vanadium-based catalysts, especially V_2O_5/TiO_2 doped with WO_3 or MoO_3, have achieved great success in selective catalytic reduction (SCR) of NO with NH_3 for their high activity and durability to SO$_x$ poisoning.[1–14] Nevertheless, this kind of catalyst has a relatively high price, which restricts their wide use in combustion facilities of small to middle scale. On the other hand, the blast furnace slag (BFS), which contains about 20 wt% TiO_2, is a massive solid waste from the iron-steel industry. In China, it amounts 3.6 million tons per year, and would cause serious environmental problems without efficient treatment and reuse.[15,16] Considering the reuse of BFS as a Ti source, we have for the first time proposed the production of V–W–Ti catalysts for flue gas denitration (DeNO$_x$) from the slag. The idea was confirmed to be effective to lower the cost of SCR catalysts and simultaneously provides a new pathway to fully utilize BFS.[17]

Recent studies have shown that incorporation of some metal oxides such as Al_2O_3, SiO_2, Fe_2O_3 and CeO_2 into TiO_2 support as mechanical promoters enhanced DeNO$_x$ catalytic performance of the resulting catalysts because the promoters likely improve the dispersion and thermal stability of catalytic components.[3–7,18–23] Especially, TiO_2–SiO_2 has drawn particular attention because of its induced high DeNO$_x$ activity and low SO_2 oxidation activity. The structural advantages from doping SiO_2 are its enhanced dispersion and stabilization effects on anatase TiO_2 and VO$_x$ species, together with the formation of more Brønsted acid sites needed for NO reduction.[5–7,19] As a matter of fact, the TiO_2–SiO_2 support with different TiO_2/SiO_2 ratios can be easily prepared in one step from BFS as shown by our recent work.[24] Besides providing low preparation cost as compared to methods based sol–gel or co-precipitation using pure chemicals, a distinguishing feature is its enabled high specific surface (427 m^2 g^{-1}) and better DeNO$_x$ performance in a wide temperature window of 250–400 °C for the prepared catalyst. However, the TiO_2–SiO_2 support made from BFS has to contain some unavoidable dopant oxides such as Al_2O_3 and Fe_2O_3 to challenge the understanding of relationship between structure and function of the BFS-derived DeNO$_x$ catalysts. It is thus necessary to deeply get insight into the structure of the BFS-derived catalysts for achieving their better applications.

The present work aims at revealing the structure effect of BFS-derived catalysts on their superior catalytic performance for DeNO$_x$ by SCR. Two catalysts on TiO_2–SiO_2 support but with different amounts of Al_2O_3/Fe_2O_3/SO_4^{2-} dopants were prepared from BFS by controls of H_2SO_4 concentration and pH value in

[a]State Key Laboratory of Multi-phase Complex Systems, Institute of Process Engineering, Chinese Academy of Sciences, Beijing 100190, China. E-mail: yujian@ipe.ac.cn; gwxu@ipe.ac.cn; Tel: +86-10-82629912

[b]University of Chinese Academy of Sciences, Beijing 100049, China

† Electronic supplementary information (ESI) available. See DOI: 10.1039/c7ra01252g

precipitation. The other two samples for comparison were prepared by traditional co-precipitation or sol–gel method using commercial inorganic or organic Ti/Si chemicals.[25,26] The SiO_2 content of all samples was nearly the same (about 0–10 wt%) as that in commercial SCR catalysts.[5,27] The structure of catalysts was obtained through characterizations using XRD, TG, BET, XPS, TPR, SEM, TEM and FT-IR for both fresh and spent catalysts, and the relationship between structure and dopants was clarified through correlating catalytic performance for SCR of NO by NH_3 and catalyst structure. This is further expected to deeply understand the mechanism of BFS-based $DeNO_x$ catalyts for their good performance of flue gas denitration.

2. Experimental section

2.1. Catalyst preparation

Raw materials used for TiO_2–SiO_2 preparation included blast furnace slag (BFS), titanium(IV) chloride ($TiCl_4$) and colloidal silica (30 wt% SiO_2 in water), or tetrabutyl titanate ($Ti(OC_4H_9)_4$) and tetraethyl orthosilicate ($Si(OC_2H_5)_4$). The BFS was water-quenched slag and from Panzhihua Iron & Steel Group Co., Ltd of China. Table 1 shows its composition obtained by XRF analysis. All other chemicals were all commercial products of reagent grade (Alfa Aesar). For comparison, a kind of commercial V–W–Ti SCR catalyst denoted as DKC ZERONOX® 993510537 was gotten from Chengdu Dongfang KWH Environmental Protection Catalyst Co., Ltd., China. This commercial monolithic honeycomb catalyst was crushed into powder and further evaluated to compare with the prepared catalysts.

The TiO_2–SiO_2 supports used in making $DeNO_x$ catalysts were prepared from different precursors according to the technical routes shown in Fig. S1 (see ESI†). The first support denoted as S-BFS-1 was prepared from BFS by, in succession, digesting the slag in 70 wt% H_2SO_4 at 90 °C for 3 h; hydrolyzing the resulting solution containing $TiOSO_4$/Si at pH = 1 and 110 °C for 5 h, washing the obtained H_2TiO_3 slurry using H_2O, aqueous NH_3 (10 wt%) and H_2O again, and finally drying the filter cake to obtain the TiO_2–SiO_2 support. The second BFS-based support with different amounts of Al_2O_3/Fe_2O_3/SO_4^{2-} dopants (S-BFS-2) was obtained via a similar procedure but its slag digestion used 60 wt% of H_2SO_4, hydrolysis did not have any pH adjustment and slurry washing to pH = 7 by using only distilled water. The detailed procedure for preparing the BFS-based supports can be found in our previous publications.[17,24]

Commercial Ti and Si precursors were also used to synthesize TiO_2–SiO_2 by co-precipitation and sol–gel methods. Following literature reports,[28,29] $TiCl_4$ and colloidal silica were used in co-precipitation, and the resulting precipitate was washed with distilled water and aqueous NH_3 to get S-CP-$TiCl_4$. Another TiO_2–SiO_2 support (S-SG-Organic) was made by sol–gel method from $Ti(OC_4H_9)_4$ and $Si(OC_2H_5)_4$ precursors.[5,30] All samples had the similar SiO_2 content and were calcined at 600 °C for 4 h in air to obtain catalyst supports.

With the preceding TiO_2–SiO_2 supports, all $DeNO_x$ catalysts were obtained by impregnating 5 wt% WO_3 and 2 wt% V_2O_5. The impregnation slurry was continuously stirred at 60 °C until it became a paste. Then the paste was dried at 110 °C for 10 h and calcined at 600 °C for 4 h to get the V_2O_5–WO_3/TiO_2–SiO_2 catalysts.[24] Four catalysts were prepared and denoted as BFS-1, BFS-2, CP-$TiCl_4$ and SG-Organic according to their different raw materials and synthesis methods used in preparing the TiO_2–SiO_2 supports.

2.2. Characterization and evaluation

Nitrogen adsorption/desorption isotherms were obtained using an ASAP 2020 (Micromeritics Instrument Corp.) working at 77 K. For all samples measured, they were degassed in vacuum at 150 °C for 6 h in prior to BET measurement. The Brunauer–Emmett–Teller (BET) equation was used to calculate the specific surface area (S_{BET}) from the recorded isotherms. Pore size distribution was calculated from the adsorption curve using the Barrett–Joyner–Halenda (BJH) model. The nitrogen adsorption volume at a relative pressure (P/P_o) of 0.994 was adopted in determining the pore volume and average pore size. The X-ray diffraction (XRD) pattern was performed in the 2θ angle from 10° to 90° on a D/Max-RB diffractometer (Rigaku Corp., Tokyo, Japan) having a Cu Kα radiation. FT-IR spectra were taken using a Tensor 27 (Bruker, Germany) in 400–4000 cm^{-1} with a resolution of 4 cm^{-1}. For this, 1.0 mg dry powder was dispersed into 100 mg *IR* transmissive material (KBr), which was further pressed to obtain the transparent disks used for measurement.

The bulk chemical composition of blast furnace slag and all the prepared supports were determined in an Axios X-ray fluorescence (XRF) spectrometer (PANalytical X'pert). The composition and oxidation state of elements presented on the surface of prepared catalysts were obtained using a X-ray photoelectron spectroscopy (XPS) working on an ESCALAB 250Xi electron spectrometer from Thermo Fisher Scientific Corporation (USA) using 100 W Al Kα radiation ($h\nu = 1486.6$ eV). A catalyst sample was put into its sample holder in advance and further degassed overnight at room temperature at a pressure of 10^{-9} mbar. Binding energies were corrected by referring to the binding energy 284.8 eV for C 1s. For all samples not containing carbon, such a C 1s signal in XPS spectra was from their adventitious carbon.

Surface morphology and cross-sectional structure of all prepared supports were characterized using a JSM-7001F scanning electron microscopy (SEM) of JEOL (Japan) working at an accelerating voltage of 10 kV, and further a JEM-2100 transmission electron microscopy (TEM) of JEOL working at 200 kV. All TEM samples were on a copper-supported carbon polymer grid, and a sample was formed by placing a few droplets (onto the grid) of a suspension made by dispersing ground sample into ethanol and in turn drying the droplets in room condition. The bulk and surface compositions of vanadium element in catalysts were determined using the Inductively Coupled

Table 1 Chemical composition of blast furnace slag (mass%)

TiO_2	SiO_2	MgO	CaO	Al_2O_3	Fe_2O_3	SO_4^{2-}	Others	Particle size
20.87	23.18	10.32	26.96	13.83	1.36	1.67	1.81	<0.2 mm

Plasma-Optical Emission Spectrometry (ICP-OES, ICAP 6300, USA) and Energy Dispersive X-ray Spectroscopy (EDS) attached to a JSM-7001F SEM, respectively.

Thermogravimetry (TG) coupled with differential scanning calorimetry (DSC) was conducted on a Labsys Evo STA 1600 (Setaram Instrumentation) to characterize the weight change and endothermal–exothermal characteristics of TiO_2-based supports and catalysts. The heating curves (TG/DSC) were recorded under inert atmosphere of argon at a heating rate of $10\,°C\,min^{-1}$ in the range of 30–1000 °C. The presence of sulfate species in the sample was evaluated from the weight loss in the range in which the release of SO_2 occurred. Both NH_3-TPD and H_2-TPR experiments were performed on an AutoChem II-2920s V5.02 equipment (Micromeritics Instrument Corp.) to obtain the surface acidity and redox properties of a sample. After loading 0.1 g sample into its quartz U-tube reactor and purged with He, the sample was heated from room temperature to 300 °C at $10\,°C\,min^{-1}$ and maintained at this temperature for 60 min in He. Then, the sample was cooled to 80 °C, followed by NH_3 adsorption for 1 h (10 vol% NH_3 in He), and finally heated to 600 °C at 10 °C min to obtain NH_3-TPD curve in $50\,mL\,min^{-1}$ pure He. For H_2-TPR analysis the sample was cooled to 90 °C and followed by heating it to 1000 °C at $20\,°C\,min^{-1}$ in H_2–He (10 vol% H_2) gas at $50\,mL\,min^{-1}$. The released NH_3 or consumed H_2 were continuously detected using a mass spectrometer (Proline MS, Ametek).

Catalytic activity for SCR of NO by NH_3 was evaluated in an atmospheric quartz fixed bed reactor of 15 mm in internal diameter. The tested catalyst was powder of 0.15–0.2 mm in sizes, and the used simulated flue gas contained 0.06 vol% NO, 0.048 vol% NH_3, 3 vol% O_2, 5 vol% H_2O, 0.06 vol% SO_2, and balanced with N_2. The tested model flue gases included NO–O_2–N_2, NO–O_2–H_2O–N_2 and NO–O_2–H_2O–SO_2–N_2, and for each kind of gas its total flow rate through the reactor was kept at 400 $mL\,min^{-1}$ (STP) to give a high Gas Hourly Space Velocity (GHSV) of 100 000 h^{-1}. The tested reaction temperature was in 150–500 °C and under each condition the test was last for 60 min. Molar concentrations for feeding and reacted gases were continually monitored in an ABB-AO2020 on-line flue gas analyzer (ABB). The realized NO conversion was calculated according to the measured inlet and outlet NO concentrations by

$$NO\ conversion\ (\%) = \frac{NO_{in} - NO_{out}}{NO_{in}} \times 100.$$

3. Results and discussion

3.1. Characterization of TiO_2–SiO_2 supports

XRF analysis. Table 2 shows the chemical compositions of all TiO_2–SiO_2 supports. Their SiO_2 content was all about 9.3 wt%, but the slag-based samples contained some unavoidable dopants such as Fe_2O_3, Al_2O_3 and SO_4^{2-}. With controlled hydrolytic pH and aqueous NH_3 washing (10 wt%), the S-BFS-1 support contained 1.38% Fe_2O_3, 0.59% Al_2O_3 and 0.39% SO_4^{2-}, whereas S-BFS-2 prepared without aqueous NH_3 washing had significantly less Fe_2O_3 (0.31%) and Al_2O_3 (nearly zero) but more

Table 2 Chemical composition of TiO_2–SiO_2 supports determined by XRF analysis

Support	TiO_2	SiO_2	Fe_2O_3	Al_2O_3	SO_4^{2-}	Others
S-BFS-1	87.72	9.17	1.38	0.59	0.39	0.75
S-BFS-2	87.18	9.3	0.31	—	2.97	0.24
S-CP-$TiCl_4$	90.67	9.21	—	—	0.12	—
S-SG-Organic	90.72	9.28	—	—	—	—

SO_4^{2-}. This amount variation for Fe_2O_3 and Al_2O_3 dopants in a slag-based samples were subject to the solubility of such species in hydrolytic solution with a certain pH value.[31,32] Both S-CP-$TiCl_4$ and S-SG-Organic samples contained only TiO_2 and SiO_2.

Textural characteristics. Fig. 1 and Table 3 show the results of BET analysis for all supports. Fig. 1 shows the obvious difference for all supports in the N_2 adsorption/desorption isotherms and pore size distribution (PSDs) curves. All supports exhibit irregular pore shape and type-IV isotherms in Fig. 1a (IUPAC classification) to characterize the mesoporous feature.[33,34] Both SiO_2 and other oxide dopants like Al_2O_3, Fe_2O_3 caused S-BFS-1 to have mesoporous structure with high BET area (282.30 $m^2\,g^{-1}$) and high pore volume (0.609 $cm^3\,g^{-1}$). For S-BFS-2, its high SO_4^{2-} content and low Al_2O_3 and Fe_2O_3 contents led to the meso–macro PSDs having lowered surface area (137.91 $m^2\,g^{-1}$) and pore volume (0.293 $cm^3\,g^{-1}$). The large mesopores and even macropores in 20–100 nm on S-BFS-2 might be from the packing of secondary aggregates.[28] Also, the crystalline size detected by XRD obviously increased from 11.9 nm for S-BFS-1 to 16.6 nm for S-BFS-2. All these indicated that the Al_2O_3 and Fe_2O_3 dopants possibly prohibited aggregation of crystallites to resist the reduction in surface area during high-temperature calcination and thus facilitated the formation of highly mesoporous structure.[4,8,35] However, the presence of SO_4^{2-} worked oppositely. Literature reviews[8,30,33] showed that the titania catalysts with high specific surface areas are well suited for selective catalysis because of their more available active sites. For S-CP-$TiCl_4$ and S-SG-Organic made using commercial reagents (without Al_2O_3 and Fe_2O_3 dopants), they had lowered BET area and pore volume in comparison with S-BFS-1, although S-BFS-1 had more sulfate. Especially for S-CP-$TiCl_4$ (made with the similar method as for S-BFS-1), it had the much smaller BET surface area, pore volume and pore size. Thus, there are great advantages for preparing high-surface-area TiO_2–SiO_2 supports from BFS.

XRD analysis. The XRD patterns compared in Fig. 2 show that TiO_2 in all supports presents as anatase crystal form (JCPDS 21-1272).[5,35,36] Estimation according to the Scherrer's formula based on the (101) diffraction peak found that the anatase crystallites are in sizes of 11.3–16.6 nm (see Table 3). Of them, the crystallite size of S-BFS-1 (containing Al_2O_3/Fe_2O_3 dopants) is about 11.3 nm, very close to that of pure TiO_2–SiO_2 made with organic materials. The sulfate in S-BFS-2, however, caused a slight growth of titania crystallinity to have thus its reduced BET surface area and big crystallite size, as similarly reported by M. Kobayashi et al.[37] Overall, the supports from
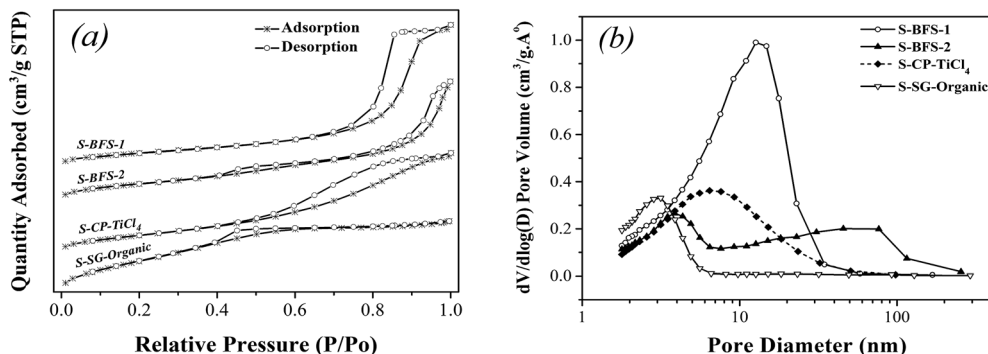
Fig. 1 Nitrogen adsorption/desorption isotherms (a) and pore size distribution (b) of TiO_2–SiO_2 supports.

BFS had high crystallinity than the samples made with organic precursors did, possibly due to the heat intolerance in calcination of the latter.[38] Thus, the origin (nature) of precursor and preparation procedure affected the crystallization characteristics of TiO_2.

Thermal analysis. Fig. 3 shows the TG and DSC profiles of calcined TiO_2–SiO_2 supports in a temperature range of 30–1000 °C with a heating rate of 10 °C min^{-1} in argon. The thermal event at 30–200 °C can be correlated to the DSC endothermic peak at around 100 °C to indicate the removal of physically adsorbed water.[31,39,40] There was not obvious weight loss and an exothermic peak when further increasing temperature to 600 °C, indicating the completion of amorphous-anatase phase transformation for all supports and there was not organic matters trapped inside the pores of S-SG-Organic.[36,41] Comparing S-BFS-1, S-CP-$TiCl_4$ and S-SG-Organic, the TG diagram of S-BFS-2 had a distinctively big weight loss peak in 550–800 °C to show the decomposition of sulfate species (see Table 2).[39,40] Besides, the DSC heating curves in 600–1000 °C revealed that varying the transition point of anatase to rutile due to the introduction of dopants showed a influence of dopants on kinetics of anatase-to-rutile transformation taking place *via* changes of oxygen vacancies in a support.[42]

SEM images. Fig. 4 displays SEM (also TEM) micrographs of all support samples. In Fig. 4a–d (SEM), all synthesized TiO_2–
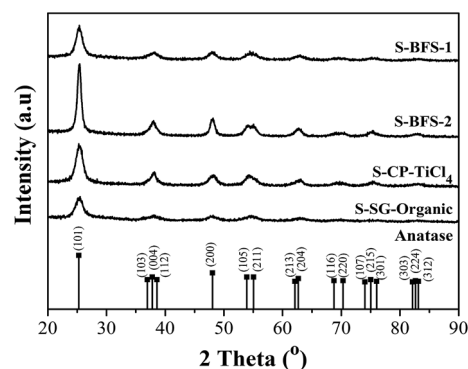

Fig. 2 XRD patterns of TiO_2–SiO_2 supports.

SiO_2 supports possess a rough porous surface, and the samples S-BFS-1 (a), S-CP-$TiCl_4$ (c) and S-SG-Organic (d) show shaped agglomerates composed of asymmetric plate-like particles. The S-BFS-2 (b) exhibits micro spherical morphology with heavy aggregation, possibly from breakage of its structure into small pieces of matters in sintering due to its high sulfate content.[43] For slag-based supports containing unavoidable Fe_2O_3 dopant, one can see a dense elemental distribution of Ti in their SEM images and EDS mappings of Ti and Fe shown in Fig. S2 and S3 (ESI†). This reveals the presence of underlying TiO_2 substrate and uniform Fe dispersion on the entire TiO_2 substrate. Their

Table 3 Textural parameters of TiO_2–SiO_2 supports calcined at 600 °C and elemental composition of their catalysts

| Sample | Textural properties of support | | | | Elemental composition of catalyst | | | | | |
| | | | | | Elemental bulk composition (ICP)[b] | | | Elemental surface composition (EDS)[c] | | |
	BET (m^2 g^{-1})	Pore size (nm)	Pore volume (cm^3 g^{-1})	Crystallite size[a] (nm)	V	Ti	V/Ti	V	Ti	V/Ti
S-BFS-1	282.30	8.62	0.609	11.9	1.151	47.17	2.44	1.72	41.14	4.18
S-BFS-2	137.91	8.50	0.293	16.6	1.147	45.68	2.51	0.93	45.2	2.06
S-CP-$TiCl_4$	164.07	6.95	0.285	13.48	1.125	46.18	2.44	1.65	57.36	2.88
S-SG-Organic	150.66	3.04	0.114	11.30	1.161	48.23	2.41	1.73	60.94	2.85

[a] Crystallite size of TiO_2 was calculated from X-ray diffraction (XRD) data. [b] Actual bulk concentration was obtained by inductively coupled plasma (ICP). [c] Surface composition was obtained from energy dispersive X-ray spectroscopy (EDS) attached to SEM.
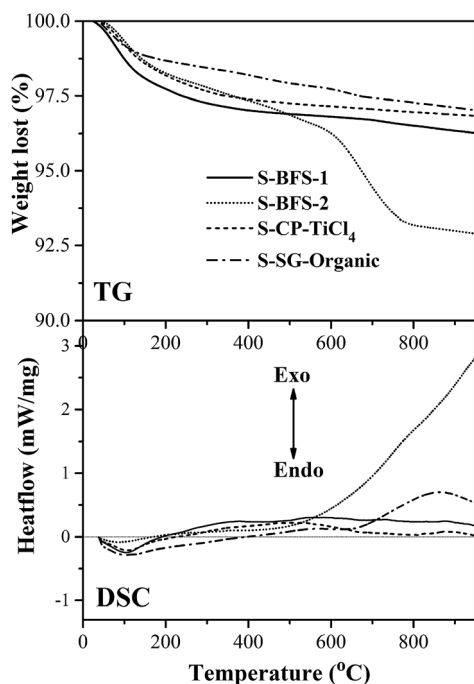
Fig. 3 TG and DSC profiles of TiO$_2$–SiO$_2$ supports at a heating rate of 10 °C min^{-1} (in argon).

EDS spectra further suggested that the ferric elements were not aggregated, complying with the absence of Fe$_2$O$_3$ peak in XRD patterns shown in Fig. 2.[13,14] Both S-CP-TiCl$_4$ and S-BFS-1, prepared *via* the same co-precipitation method, displayed the similar morphology to indicate that starting material has not obvious effect on morphology of the resulting support. Overall, the surface morphology of synthesized support obviously varied with the treatment method, either co-precipitation or sol–gel synthesis. The particles from sol–gel method (S-SG-Organic) showed some layered stacking structure with less rough surface than the co-precipitation method did.[44]

TEM images. As shown by TEM images in Fig. 4e–h, all TiO$_2$–SiO$_2$ supports had spherical primary particles without any coating on surface.[31] Mesopore structure features can be clearly seen to indicate high surface area and high adsorptive capacity.[35,38] The S-BFS-1 had the best dispersion to show small particle sizes, while serious aggregation occurred to S-BFS-2 to form large particle sizes. The results well agree with the BET results in Fig. 1. For all samples, SiO$_2$ particles and impurities were not clearly identified and their non-uniform distributions were observed in the TEM images. A high-resolution transmission electron microscopic study (HR-TEM) was performed to observe the distribution of crystalline titania (Fig. S2–S5(a) in ESI†). All the observed lattice fringes of TiO$_2$–SiO$_2$ nanoparticles show a *d*-spacing of 0.360 nm, just corresponding to the (101) lattice fringes of anatase TiO$_2$ (*d* = 0.352 nm, JCPDS No. 21-1272).[35,38] In summary, one can see from the TEM and SEM images that the dopants and synthetic route remarkably affected the morphologies and nano-micron structure of the prepared TiO$_2$–SiO$_2$ supports, and the S-BFS-1 support had the best dispersion of its precursors.
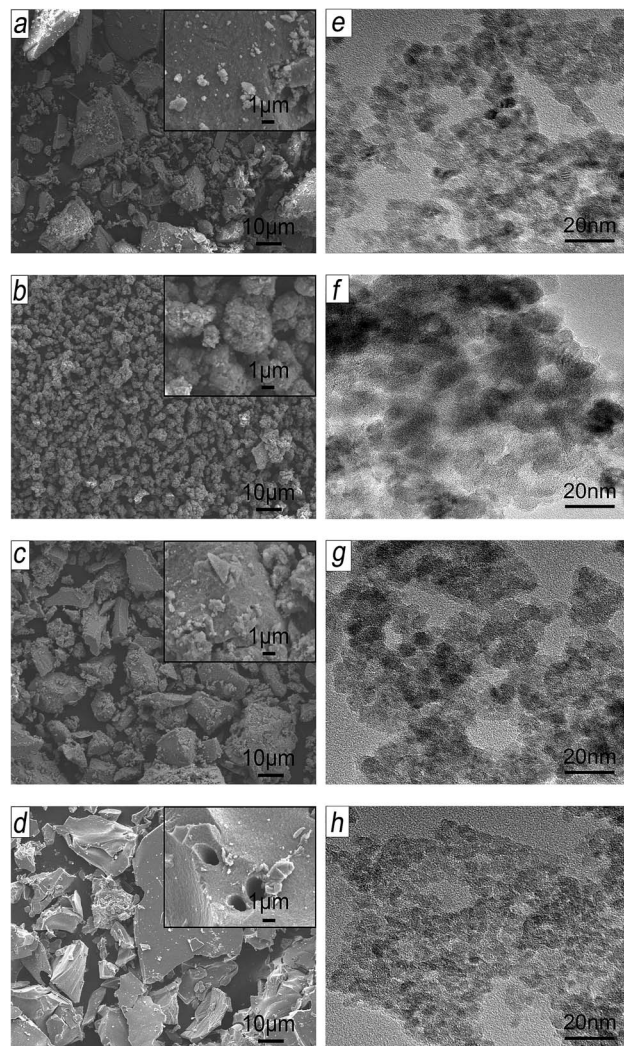

Fig. 4 SEM and TEM images of S-BFS-1 (a, e), S-BFS-2 (b, f), S-CP-TiCl$_4$ (c, g) and S-SG-Organic (d, h).

FT-IR analysis. The FT-IR spectra in Fig. 5 for all supports demonstrate a large and intense band within 3200–3600 cm^{-1} to indicate the presence of OH group on TiO$_2$–SiO$_2$ surface and also a sharp peak at 1635 cm^{-1} to refer to the O–H stretching vibration in water. The broad adsorption peak located in 400–
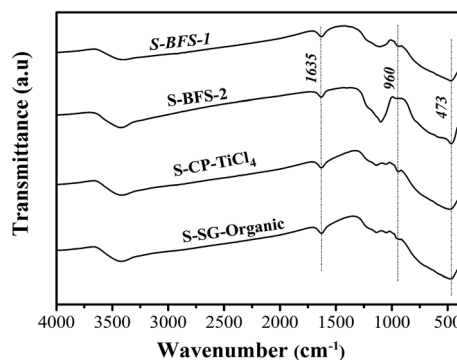

Fig. 5 FTIR spectra of TiO$_2$–SiO$_2$ supports.

600 cm^{-1} represents the characteristic vibration of Ti–O bonds in Ti–O–Ti.[5,35,45] An absorption band extending from 1000 to 1300 cm^{-1} shows the asymmetric and symmetric stretching of Si–O–Si bridge, and a minor feature around 960 cm^{-1} can be associated with the vibrations of Si–O–Ti linkage. Thus, a substitution of Si for Ti has occurred in the prepared TiO$_2$–SiO$_2$ supports.[35,45] Besides, the absorption band within 1000–1300 cm^{-1} is more intensive for the sulfated S-BFS-2 sample, indicating the vibration overlapping of Si–O–Si and S=O bonds, where the latter is associated with sulfate groups and anchored to TiO$_2$–SiO$_2$ surface.[39,46]

In summary, the supports made with the co-precipitation method, as compared to the sol–gel synthesis, displayed the similar morphological features and their rough porous surface provided the larger surface area. On the other hand, the dopants also greatly influenced the structure of synthesized TiO$_2$–SiO$_2$ such as size of crystallites, porous textures and particle agglomeration. The dopants Al$_2$O$_3$ and Fe$_2$O$_3$ (as in S-BFS-1) facilitated mesoporous structure, enlarged BET surface area as well as mesoporous size because they inhibited the growth of anatase TiO$_2$ grain by their existence on TiO$_2$ boundary. The presence of SO$_4^{2-}$ made the TiO$_2$–SiO$_2$ support easy to agglomerate to form meso–macro pores, having thus the obviously low surface area for S-BFS-2. These difference in porosity, surface area and crystallinity parameters of TiO$_2$–SiO$_2$ supports will greatly impact the catalysts made with them for SCR of NO with NH$_3$ (flue gas DeNO$_x$).

3.2. Evaluation of catalysts for DeNO$_x$

Denitration catalysts were prepared by impregnated 2 wt% V$_2$O$_5$ and 5 wt% WO$_3$ onto the preceding TiO$_2$–SiO$_2$ supports having different structures, properties and Fe$_2$O$_3$/Al$_2$O$_3$/SO$_4^{2-}$ dopants amounts. The SEM images and EDS spectra as well as mappings of Ti/V elements in Fig. S2–S5(b–e) shown in ESI† confirmed that all prepared V$_2$O$_5$–WO$_3$/TiO$_2$–SiO$_2$ catalysts were composed of Ti, Si, Al, Fe, O, V, W elements, and the main active element V was highly dispersed into the lattice of entire TiO$_2$ substrate.[14] The ICP-OES and EDS results shown that all the catalysts had the similar bulk vanadium contents of about 1.1 wt% but different surface V concentrations (Table 3), showing essentially the varied interactions between V$_2$O$_5$ and support for different catalysts.[13,14] In the following, DeNO$_x$ performance was evaluated to correlate the structure and dopants of supports with the catalytic performance for SCR of NO by NH$_3$.

Fig. 6 shows the results of DeNO$_x$ performance over catalysts prepared using the preceding supports. At the same reaction conditions, all prepared catalysts except for BFS-2 enabled higher NO reduction than the reference DKC commercial catalyst did in the reaction temperature of 250–450 °C. The realized NO removal over DKC below 70% but it had a acceptably wide temperature window for DeNO$_x$. The BFS-1 catalyst exhibited the best catalytic activity by having about 74% NO conversion in 300–450 °C under an NH$_3$/NO ratio of 0.8 and GHSV of 100 000 h^{-1}. The manifested activity for CP-TiCl$_4$ was between BFS-1 and SG-Organic catalysts. Although BFS-2 contained the highest sulfate, it showed the lowest activity among
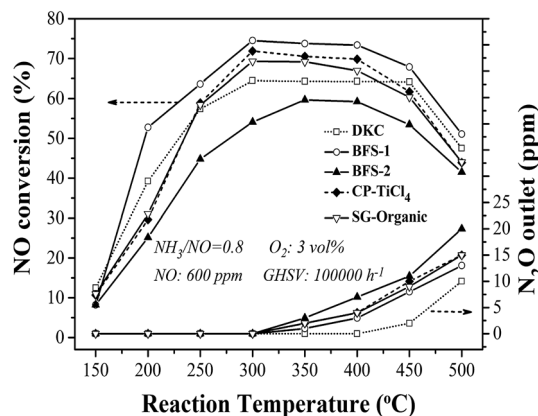

Fig. 6 NO conversion and N$_2$O formation varying with reaction temperature for prepared and commercial DKC catalysts.

all prepared catalysts. Referring to the support compositions in Table 2, one can conclude that the proper amounts of Fe$_2$O$_3$ and Al$_2$O$_3$ dopants in catalytic support facilitated NH$_3$-SCR reactions over V$_2$O$_5$–WO$_3$/TiO$_2$–SiO$_2$ catalysts. Earlier studies have shown that the incorporation of Al$_2$O$_3$ (ref. 20, 21 and 47) of up to 10 wt% and Fe$_2$O$_3$ (ref. 4, 11 and 48) of up to 3 wt% into the TiO$_2$ support are beneficial to NO reduction in NH$_3$-SCR, and the catalyst has better thermal stability in comparison with conventional V$_2$O$_5$/TiO$_2$ catalysts. Thus S-BFS-1 support should be a promising candidate for making inexpensive and highly active catalyst for flue gas DeNO$_x$. Also, one can infer that the activity for DeNO$_x$ of TiO$_2$–SiO$_2$ supported catalysts was mainly subject to the dopants in support other than the precursors (materials) and preparation method. The presence of Fe$_2$O$_3$ (ref. 4 and 11) and Al$_2$O$_3$ (ref. 20 and 21) would positively work on DeNO$_x$ performance of the resulting catalyst, but too much SO$_4^{2-}$ (about 3 wt%) in support would lead to adverse impacts. Literature studies[37,49,50] have reported that the presence of about 1 wt% sulfate in TiO$_2$ and TiO$_2$–SiO$_2$ supports would promote NH$_3$-SCR performance of the resulting catalyst because of its increase in catalyst acidity and facilitation in oxidation of NO into nitrate and transformation of monomeric vanadate into polymeric vanadate on catalyst surface.

The generation of N$_2$O during NH$_3$-SCR was also tested. At temperatures above 350 °C, ammonia would be partially oxidized to N$_2$O,[3,7] but only negligible N$_2$O (3 ppm) was formed at 450 °C over DKC (see Fig. 6). The formed N$_2$O amount at 350–500 °C over all catalysts followed a sequence of BFS-2 > CP-TiCl$_4$ ≈ SG-Organic > BFS-1 > DKC. In term of composition and structure features, the low emission of N$_2$O at high temperatures over BFS-1 catalyst should be related to its presence of Al$_2$O$_3$ and Fe$_2$O$_3$ dopants. Hence, the type of dopants is critical to achieve the expected high N$_2$ selectivity of catalyst for SCR of NO by NH$_3$.

The tolerance to poisoning of SO$_2$ and steam was tested by feeding 5 vol% steam and 600 ppm SO$_2$ at 300 °C in a stable SCR reaction lasting for a few hours under GHSV of 100 000 h^{-1}. As shown in Fig. 7, the presence of both SO$_2$ and H$_2$O in the reactant (fed) gas caused obvious loss of DeNO$_x$ activity from the case with only H$_2$O (steam) feed. Having only 5 vol% H$_2$O in gas
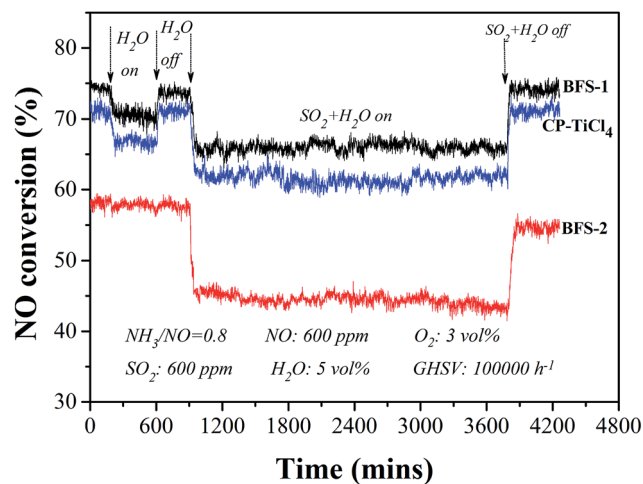
Fig. 7 Stability tests of BFS-1, BFS-2 and CP-TiCl$_4$ catalysts for SCR of NO by NH$_3$ at 300 °C.

the absolute drop of NO conversion was 2.6%, 3.5% respectively over the BFS-1, CP-TiCl$_4$ catalysts, meanwhile the deactivation nearly was not seen over sulfated TiO$_2$–SiO$_2$ supported catalyst (BFS-2). The interaction of sulfate species with adsorbed water can cause the formation of Brønsted acid sites to promote the NH$_3$ adsorption, which may compensate the degree of the loss of its DeNO$_x$ efficiency.[39,51] Stopping H$_2$O feed, NO conversions were fully reversible for all catalysts, indicating that this inhibition is due to competitive adsorption of H$_2$O and NH$_3$ on active sites.[1,46]

Feeding SO$_2$ and steam simultaneously revealed that the realized NO conversion was stable but further dropped by 8%, 10% respectively for BFS-1 and CP-TiCl$_4$ catalysts from the flue gas without presence of SO$_2$ and steam, furthermore shutting off the feeding of both SO$_2$ and steam, their DeNO$_x$ activity were recovered quickly to their initial high value. At the analogous reaction conditions, the activity over BFS-2 dropped by 12.7% and decreased gradually afterwards, besides its recovery of catalytic performance was gradual and the performance could not rebound to the original after cutting off SO$_2$ and steam in fed gas. Thus, high sulfate content in catalyst is not good for tolerance to the poisoning of steam and SO$_2$ because the formed Brønsted acid sites and long-term exposure to SO$_2$ containing in flue gas can lead to the formation of ammonium sulfates (NH$_4$HSO$_4$ and (NH$_4$)$_2$SO$_4$) on catalysts easily,[1,2,30,46] which would cause similar deactivation for all catalysts. In summary, the impurities Al$_2$O$_3$/Fe$_2$O$_3$ (excluding SO$_4^{2-}$) not only enhanced DeNO$_x$ activity and selectivity of the prepared catalyst but also positively affected the resistance of the catalyst to poisoning by water and SO$_2$ in SCR of NO.[20,52] Obviously, BFS-1 is the most active and robust catalyst for DeNO$_x$ application to actual flue gases.

Correlating with structure of catalyst supports found that the preceding catalytic activities for DeNO$_x$ increased with increasing the surface area of supports. Indeed, large pore volume and high surface area of a catalyst would improve its catalytic activity by facilitating spread of reactant molecules

(NO) or reaction intermediates to active sites in catalyst's meso-structure framework.[30,33,53] The catalyst BFS-1 showed high NO reduction capability (about 74% reduction) at 300–450 °C under high GHSV of 100 000 h^{-1}. Agglomeration observed on BFS-2 reduced its BET surface and also blocked some active sites, which caused thus the instability of the catalyst in gas containing both of steam and SO$_2$.[43] Thus, the texture and morphology of support importantly affect the catalytic performance of V$_2$O$_5$–WO$_3$/TiO$_2$–SiO$_2$ for DeNO$_x$ by NH$_3$. The BFS-1 catalyst with the relatively low crystallinity exhibited the best DeNO$_x$ activity, possibly owing to its special acid sites and large BET surface area to have highly dispersed vanadia on catalyst surface, as further justified below.

3.3. Justification of catalytic activities

NH$_3$-TPD. Comparing the profiles of temperature programmed desorption of ammonia (NH$_3$-TPD) in Fig. 8 shows clearly different acidic sites for catalysts having different contents of Al$_2$O$_3$/Fe$_2$O$_3$/SO$_4^{2-}$ dopants. While BFS-2 containing high SO$_4^{2-}$ content displayed two broad NH$_3$ desorption regions below and above 400 °C to refer to weak and strong acid sites, the other catalysts exhibited only one broad and asymmetric peak below 400 °C to represent weak acid sites.[20,35,45] The clarification in Fig. 8 and data in Table 4 show actually that the impurities in slag-based catalysts caused strong acidic sites on catalyst surface in comparison with those prepared from commercial Ti/Si sources. The highest amount of desorbed NH$_3$ occurred at temperatures of 100–400 °C for BFS-1. For BFS-2 its strong acidic sites occurred at 400–600 °C due to the strong interaction between sulfate anion and titanium cation which causes the titanium cation to be more positively charged ions. Accordingly there were few weak acid sites for BFS-2, showing that the strong acid sites are formed by reducing weak acid sites,[8,54] causing strong adsorption and oxidation of NH$_3$ to hinder the SCR reaction for NO as evidenced in Fig. 6.[7,37,49] Weak acidic sites are beneficial to DeNO$_x$ activity by their retaining of NH$_3$ for SCR reaction.[5,7,36] This was confirmed by correlating the DeNO$_x$ activity and amount of weak acid sites such that BFS-1 had the highest amount of weak acid sites and also the best DeNO$_x$ performance. The presence of unavoidable sulfate species in CP-TiCl$_4$ prepared by co-precipitation using H$_2$SO$_4$
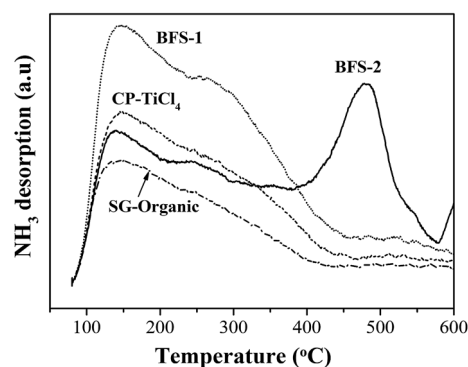

Fig. 8 TPD profile of NH$_3$ on V$_2$O$_5$–WO$_3$/TiO$_2$–SiO$_2$ catalysts.

Table 4 Results of NH$_3$-TPD and H$_2$-TPR experiments for all prepared DeNO$_x$ catalysts

| Catalyst	Acidity: NH$_3$ desorption (mmol g^{-1})			Redox properties: H$_2$ consumption (mmol g^{-1})		
	Weak acid	Strong acid	Total	VO$_x$ reduction	WO$_x$ reduction	Total
BFS-1	0.317	—	0.317	0.316	0.126	0.442
BFS-2	0.073	0.075	0.148	0.299	0.071	0.370
CP-TiCl$_4$	0.210	—	0.210	0.158	0.169	0.327
SG-Organic	0.139	—	0.139	0.122	0.067	0.189

acid caused more adsorbed NH$_3$ to participate in SCR reaction and had thus higher NO$_x$ reduction than SG-Organic catalyst did. In summary, the difference in DeNO$_x$ activity for all compared catalysts having the same SiO$_2$ content should be correlative with their different weak acidities that determine the ability to retain adsorbed NH$_3$.[5,36] For S-BFS-1, its high BET surface area acquired from its Al$_2$O$_3$/Fe$_2$O$_3$ dopants and proper sulfate content (0.4 wt%) caused the catalyst to have abundant weak acid sites and thus good DeNO$_x$ performance. The too much SO$_4^{2-}$ in support can convert a part of weak acid sites into inert strong acidic sites to decrease DeNO$_x$ activity as S-BFS-2 performed.[7,37]

H$_2$-TPR. Fig. 9 shows the H$_2$-TPR diagrams for all catalysts, and their corresponding amounts of consumed H$_2$ were summarized in Table 4. A two-step reduction profile was observed with their T_{max} at 431–471 °C and 718–863 °C and representations of active V$_2$O$_5$ and promoter WO$_3$, respectively.[3–5] The samples made from slag exhibited the larger reduction peak, indicating the more reducible metal oxides on catalyst surface or the higher reducibility for slag-based catalysts.[3,5,55] On the other hand, the shift of reduction peak for active VO$_x$ reflects the difficulty in changing its valence during DeNO$_x$ reactions.[5,36] The lower reduction temperature of VO$_x$ species, the higher catalytic activity was achieved.[3,5] For BFS-1, it had the lowest T_{max} to reduce VO$_x$ species and the highest H$_2$ consumption in H$_2$-TPR, indicating its more reducible active VO$_x$ species and thus higher DeNO$_x$ efficiency clarified in Fig. 6. In comparison, the BFS-2 catalyst with the highest T_{max} for reducing VO$_x$ species manifested the worst DeNO$_x$ performance so that CP-TiCl$_4$ and SG-

Organic catalysts had the intermediate catalytic activity for DeNO$_x$ to respond their intermediate T_{max} for reducing VO$_x$ species. Considering its high BET surface area, the low reduction temperature and many reducible sites for BFS-1 may be owing to its highly dispersed VO$_x$ species on catalyst surface.[8,30,33]

XPS. Fig. 10a–d show the electron binding energies of Ti 2p, Si 2p, O 1s and V 2p XPS peaks of V$_2$O$_5$–WO$_3$/TiO$_2$–SiO$_2$ catalysts determined using XPS analysis. All peaks were fitted by Gaussian–Lorentz curves. One may see that the reported electron binding energies agree well with other reports.[5,25,26,35,45,56] From the XPS spectra of Ti 2p in Fig. 10a we can see that the binding energies (BE) of Ti 2p$_{3/2}$ and Ti 2p$_{1/2}$ refer to Ti^{4+} in TiO$_2$, which are respectively higher than 458.7 and 464.4 eV for pure TiO$_2$.[5,35,45] A downward shift (to be slightly lower) of Si 2p BE was detected in Fig. 10b, as compared to 103.4 eV for pure SiO$_2$,[5,35] which indicates a decrease in the effective positive charge on Si. These essentially revealed the strong interaction between TiO$_2$ and SiO$_2$ in TiO$_2$–SiO$_2$ support. Since Ti has greater affinity to oxygen than Si does, some Si–O bands disappeared to promote the formation of Ti–O bands on surface and thus to reduce the binding energy of Si 2p. Combining the results of XPS and FT-IR (Fig. 5) suggests the formation of Ti–O–Si linkages in the prepared catalyst, as also reported elsewhere.[25,26] There were obvious upward shift of Ti 2p and downward shift of Si 2p for BFS-1 in comparison with the other three samples, referring to more Ti–O–Si linkages and better interspersion of Ti–Si components in this support. This well accounts for the high BET area, small particle size and weak crystallization for BFS-1.[7,25,26]

Fig. 10c shows interesting feature of O 1s XPS spectra. All catalysts are characterized by complex profiles to indicate the presence of different oxygen chemical bonds. The BE around 533 eV is attributed to the surface adsorbed oxygen (denoted as O$_{ads}$), such as O$_2^{2-}$ or O$^-$ belonging to defect-oxide or hydroxyl-like group. Another peak located around 530 eV corresponds to the lattice oxygen atom O^{2-} (denoted as O$_{lat}$), indicating a mainly single chemical environment surrounding the photo emitting oxygen.[25,26] Against the O$_{lat}$ for catalyst based on pure TiO$_2$, the upward shifts in BE of O 1s peak for all other catalysts clarified a substitution of Ti atoms by other higher electronegativity elements like Si, Al, Fe, S.[5,25,26] For BFS-2, the upward shift of O 1s peak was more pronounced, as recognized from the broad O$_{ads}$ peak, which reflects a more electronegative environment around oxygen atom due to the strong electron affinity by S^{6+} in SO$_4^{2-}$.
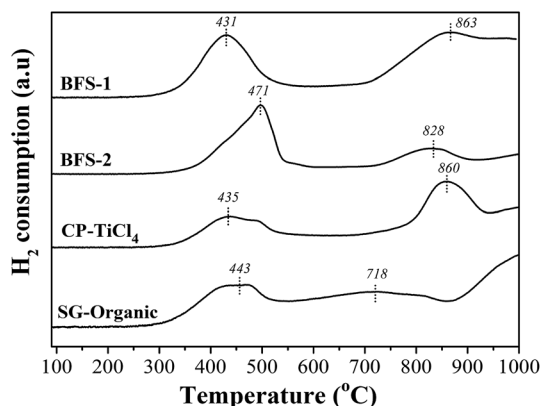
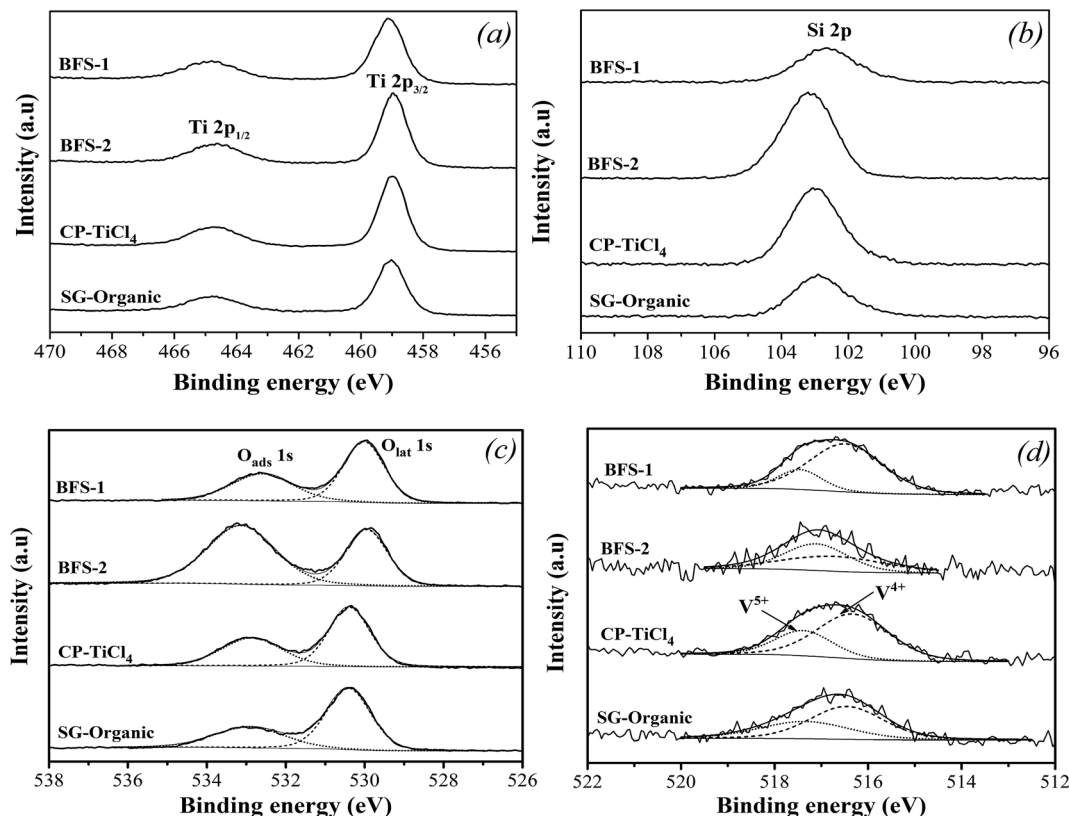**Fig. 9** H$_2$-TPR profile of V$_2$O$_5$–WO$_3$/TiO$_2$–SiO$_2$ catalysts.

Fig. 10 XPS spectra of Ti 2p (a), Si 2p (b), O 1s (c) and V 2p (d) in TiO_2–SiO_2 based catalysts.

Table 5 shows the surface O_{ads}/O ratios of all samples. The slag-based catalysts had notably high O_{ads}/O ratios. The more O_{ads} on surface should result from the more defects created by the Al_2O_3, Fe_2O_3, SO_4^{2-} dopants. The O_{ads} is usually considered to be beneficial for NO oxidation into NO_2 in SCR reactions, thereby facilitating "fast SCR" reaction and enhancing $DeNO_x$ efficiency at low temperatures.[5,18] Thus, the more surface adsorbed oxygen O_{ads} should be responsible for the better catalytic performance of BFS-1. However, a very high O_{ads}/O ratio, such as for BFS-2, means an excessive oxidation ability, which is harmful to SCR reaction owing to its induced strong ammonia oxidation that forms nitrogen oxide byproducts to narrow the temperature window of SCR and to generate more N_2O (Fig. 6).[56]

The XPS spectra in Fig. 10d presents the chemical states of vanadium. In all prepared catalysts, two peaks representing V^{5+} and V^{4+} were detected in the range of 516.4–517.1 eV and 515.7–516.2 eV, respectively.[5,7] Table 5 listed surface atom concentrations and peak-fitting results of O 1s and V 2p spectra. We can see that BFS-1 had the highest surface V to indicate the best dispersion of vanadium species in the catalyst. Combining with the BET results in Fig. 1, the surface V signals are well related with the BET area of the four catalysts, meaning that high BET area is in favor of dispersion and exposure of vanadium species. Moreover, the non-stoichiometric V^{4+} species can improve the NO reduction ability of catalyst due to its high mobility and activation of electron transfer.[5,7,21] Consequently, the realized $DeNO_x$ efficiency for all catalysts are proportionally correlated with the amount of V^{4+} ratio on their surfaces shown in Table 5. The BFS-1 catalyst had the highest BET area, best dispersion of surface vanadium species and largest V^{4+}/V ratio, thus it was rich in active vanadium sites on its surface to ensure its good catalytic performance in SCR of NO. Furthermore, Table 3 shows that the surface V/Ti ratio of BFS-1, CP-TiCl_4 and SG-Organic catalysts were higher than their bulk ratios, suggesting that V_2O_5 was mainly dispersed on their catalyst surface. The surface V/Ti ratio of BFS-2 was lower than its bulk ratio, implying that its vanadium mainly existed in the inside of catalysts.[57] The BFS-2 catalyst had consequently poor $DeNO_x$ performance as was tested.

Spent catalyst analysis. Table 6 summarized the textural characteristics (S_{BET} and V_{pore}) of fresh and spent BFS-1, BFS-2 and CP-TiCl_4 catalysts, where the spent ones refer to 70 h

Table 5 Surface elemental composition (% atomic concentration) and atomic ratios of prepared catalysts

Catalyst	Surface atomic concentration (at.%)					Surface atomic ratios[a], %	
	Ti 2p	Si 2p	O 1s	V 2p	W 4f	O_{ads}/O	V^{4+}/V
BFS-1	22.28	9.86	64.78	0.82	2.26	48.24	80.37
BFS-2	13.18	19.09	66.26	0.24	1.23	63.02	48.89
CP-TiCl_4	20.63	11.26	65.51	0.68	1.93	40.96	69.15
SG-Organic	19.46	12.17	65.19	0.65	2.53	34.83	60.66

[a] Calculated from the ratio of peak area of XPS spectra.

Table 6 Properties of spent catalysts after exposure to SO$_2$ and steam at 300 °C for 70 h

Catalyst	Fresh catalysts		Spent catalysts			
	Surface area (m^2 g^{-1})	Pore volume (cm^3 g^{-1})	Surface area (m^2 g^{-1})	Pore volume (cm^3 g^{-1})	TG loss in 250–550 °C (%)	TG loss for >550 °C (%)
BFS-1	144.86	0.436	133.64	0.409	—	3.6
BFS-2	115.63	0.290	90.22	0.218	4.0	7.5
CP-TiCl$_4$	136.42	0.270	121.43	0.232	—	3.8

exposure to SO$_2$ and steam at 250 °C. They all showed decrease in catalyst surface area, corresponding to the drop in catalytic activity when exposed to SO$_2$ and steam. There should be some solid materials formed during SCR reaction in flue gas containing SO$_2$ and H$_2$O, which blocks or collapses pores of catalyst.[2,22,30,33] The more decrease in pore volume would lead to more deactivation species deposited on catalyst.[2] There are two possible kinds of such deactivation species. The reaction between SO$_2$ or sulfate and NH$_3$ forms (NH$_4$)$_2$SO$_4$ and NH$_4$HSO$_4$ at low temperatures to block pores by deposition, while some active metal oxides may be sulfated by SO$_2$ to form stable sulfate species to destroy pore structure.[2,9,22,58]

The most serious poisoning suffering for BFS-2 in Fig. 7 was further verified by the high amount of sulfate existing on its spent catalyst (see TG data in Table 6). The weight loss at 250–550 °C represents the decomposition of ammonium sulfate salts,[22] which was observed only for spent BFS-2 catalyst. Considering its high SO$_4^{2-}$ content and abundant strong acid sites in 400–600 °C shown by NH$_3$-TPD experiment, this catalyst is easier to accommodate irreversible ammonium salts during SCR of NO, which thus decreased catalyst lifetime and was hard to regenerate. The meso–macro PSDs of BFS-2 would also facilitate accommodation of ammonium salts during SCR.[58] For mesoporous BFS-1 and CP-TiCl$_4$ catalysts that had only weak acid sites, their ammonium salts in pores could be evaporated to greatly restore blocked pores and surfaces, thereby recovering their DeNO$_x$ activity after stopping the SO$_2$ and steam feed into the tested flue gas. The mass loss occurred at 500–850 °C provided an evidence for the sulfate ions incorporated into TiO$_2$ lattice (stable metal sulfates). This also decreased the pore volume of catalysts, especially for spent BFS-2, and suggested structure damage and irreversible deactivation of BFS-2 catalyst for SCR of NO.[9]

As a summary, we can see that all spent catalysts lost their surface area in comparison with their fresh catalysts due to the formation of sulfate salts, especially for BFS-2 catalyst. This is the primary reason for the irreversible deactivation of catalyst for SCR of NO. On the other hand, too much doped SO$_4^{2-}$ in catalyst such as BFS-2 and too many strong acid sites would cause serious generation of ammonium sulfate species to block active sites and collapse pore structure of catalyst. With suitable content of SO$_4^{2-}$ dopant (below 1 wt%) in BFS-1, it increased NH$_3$ adsorption capacity and surface O$_{ads}$/O ratio to improve the DeNO$_x$ performance.

4. Conclusions

Four V$_2$O$_5$–WO$_3$/TiO$_2$–SiO$_2$ samples with different amounts of Al$_2$O$_3$/Fe$_2$O$_3$/SO$_4^{2-}$ dopants prepared from blast furnace slag (BFS) containing Ti/Si and also commercial Ti/Si sources were characterized to reveal the relationship among performance, structure and preparation method of catalyst. Results shown that the BFS-based catalysts with proper amounts of Al$_2$O$_3$/Fe$_2$O$_3$/SO$_4^{2-}$ dopants exhibited excellent catalytic activity, selectivity and stability to ensure the high NO reduction capability (about 74% reduction) at temperatures of 300–450 °C and NH$_3$/NO ratio of 0.8. The performance is much better than that realized by the catalyst made by co-precipitation or sol–gel methods using commercial Ti/Si sources. Characterization demonstrated that the Al$_2$O$_3$/Fe$_2$O$_3$ dopants acquired from using BFS prevented agglomeration of Ti–Si composite oxides and facilitated the formation of abundant Ti–O–Si linkages that led to good interspersion of Ti–Si components and high surface area of the resulting TiO$_2$–SiO$_2$ support. Reflecting on catalyst, the high surface area of TiO$_2$–SiO$_2$ support facilitated dispersion of active surface vanadium species, lowered reduction temperature of vanadium oxides and provided sufficient weak acid sites to create enough active surface V sites for high NH$_3$ adsorption capacity and active catalytic activity in SCR of NO over the catalyst. On the other hand, the proper amount of Al$_2$O$_3$/Fe$_2$O$_3$/SO$_4^{2-}$ dopants in a catalyst can also create more defects in its TiO$_2$–SiO$_2$ support to generate adsorptive O (O$_{ads}$ species) on the catalyst surface which is required for fast SCR reaction and high DeNO$_x$ efficiency. A small amount of SO$_4^{2-}$ in catalyst would increase the weak acid sites and form proper O$_{ads}$ species on the surface, whereas too high content of SO$_4^{2-}$ caused agglomeration of TiO$_2$–SiO$_2$ particles to form many strong acid sites and too many O$_{ads}$ species. The latter actually led to severe oxidation of NH$_3$ and obvious formation of stable sulfate salts to decrease consequently the DeNO$_x$ activity, selectivity and lifetime of the corresponding catalyst. Overall, the article demonstrated excellent DeNO$_x$ performances for a catalyst made using BFS because of its presence of proper amounts of Al$_2$O$_3$/Fe$_2$O$_3$/SO$_4^{2-}$ as the catalyst dopants or impurities from processing Ti-bearing BFS in making the catalyst. In fact, such dopants indeed obviously modified the support properties and chemical variability of active vanadium species, as was shown by the preceding results.

Acknowledgements

References

1 W. Shan and H. Song, *Catal. Sci. Technol.*, 2015, **5**, 4280–4288.

2 Y. Zheng, A. D. Jensen and J. E. Johnsson, *Appl. Catal., B*, 2005, **60**, 253–264.

3 C. Wang, S. Yang, H. Chang, Y. Peng and J. Li, *Chem. Eng. J.*, 2013, **225**, 520–527.

4 R. Gao, D. Zhang, X. Liu, L. Shi, P. Maitarad, H. Li, J. Zhang and W. Cao, *Catal. Sci. Technol.*, 2013, **3**, 191–199.

5 Y. Pan, W. Zhao, Q. Zhong, W. Cai and H. Li, *J. Environ. Sci.*, 2013, **25**, 1703–1711.

6 M. Kobayashi, R. Kuma and A. Morita, *Catal. Lett.*, 2006, **112**, 37–44.

7 M. Kobayashi, R. Kuma, S. Masaki and N. Sugishima, *Appl. Catal., B*, 2005, **60**, 173–179.

8 W. Cha, S.-T. Yun and J. Jurng, *Phys. Chem. Chem. Phys.*, 2014, **16**, 17900–17907.

9 Z. Ma, X. Wu, Y. Feng, Z. Si, D. Weng and L. Shi, *Prog. Nat. Sci.*, 2015, **25**, 342–352.

10 L. Chen, J. Li and M. Ge, *J. Phys. Chem. C*, 2009, **113**, 21177–21184.

11 S. Yang, C. Wang, L. Ma, Y. Peng, Z. Qu, N. Yan, J. Chen, H. Chang and J. Li, *Catal. Sci. Technol.*, 2013, **3**, 161–168.

12 S. S. R. Putluru, L. Schill, A. Godiksen, R. Poreddy, S. Mossin, A. D. Jensen and R. Fehrmann, *Appl. Catal., B*, 2016, **183**, 282–290.

13 K. Cheng, J. Liu, Z. Zhao, Y. Wei, G. Jiang and A. Duan, *RSC Adv.*, 2015, **5**, 45172–45183.

14 W. Cha, S. Chin, E. Park, S.-T. Yun and J. Jurng, *Appl. Catal., B*, 2013, **140–141**, 708–715.

15 D.-s. Chen, L.-s. Zhao, T. Qi, G.-p. Hu, H.-x. Zhao, J. Li and L.-n. Wang, *Trans. Nonferrous Met. Soc. China*, 2013, **23**, 3076–3082.

16 L. Zhang, L. N. Zhang, M. Y. Wang, G. Q. Li and Z. T. Sui, *Miner. Eng.*, 2007, **20**, 684–693.

17 J. Yang, S. Lei, J. Yu and G. W. Xu, *J. Environ. Chem. Eng.*, 2014, **2**, 1007–1010.

18 K. Cheng, J. Liu, T. Zhang, J. Li, Z. Zhao, Y. Wei, G. Jiang and A. Duan, *J. Environ. Sci.*, 2014, **26**, 2106–2113.

19 Y. Peng, C. Liu, X. Zhang and J. Li, *Appl. Catal., B*, 2013, **140–141**, 276–282.

20 W. Zhao, Y. Tang, Y. Wan, L. Li, S. Yao, X. Li, J. Gu, Y. Li and J. Shi, *J. Hazard. Mater.*, 2014, **278**, 350–359.

21 H. K. Matralis, M. Ciardelli, M. Ruwet and P. Grange, *J. Catal.*, 1995, **157**, 368–379.

22 X. Zhao, L. Huang, S. Namuangruk, H. Hu, X. Hu, L. Shi and D. Zhang, *Catal. Sci. Technol.*, 2016, **6**, 5543–5553.

23 L. Yan, Y. Liu, H. Hu, H. Li, L. Shi and D. Zhang, *ChemCatChem*, 2016, **8**, 2267–2278.

24 T. Tran, J. Yu, L. Gan, F. Guo, D. Phan and G. Xu, *Catalysts*, 2016, **6**, 56.

25 X. Gao and I. E. Wachs, *Catal. Today*, 1999, **51**, 233–254.

26 H. S. Kibombo, R. Peng, S. Rasalingam and R. T. Koodali, *Catal. Sci. Technol.*, 2012, **2**, 1737–1766.

27 M. Casanova, K. Schermanz, J. Llorca and A. Trovarelli, *Catal. Today*, 2012, **184**, 227–236.

28 O. Ruzimuradov, S. Nurmanov, Y. Kodani, R. Takahashi and I. Yamada, *J. Sol-Gel Sci. Technol.*, 2012, **64**, 684–693.

29 W. Li and T. Zeng, *PLoS One*, 2011, **6**, e21082.

30 W. Zhao, Q. Zhong, T. Zhang and Y. Pan, *RSC Adv.*, 2012, **2**, 7906–7914.

31 Z. Li, Z. Wang and G. Li, *Powder Technol.*, 2016, **287**, 256–263.

32 F. Valighazvini, F. Rashchi and R. K. Nekouei, *Ind. Eng. Chem. Res.*, 2013, **52**, 1723–1730.

33 T. J. Pinnavaia, T. R. Pauly and S. S. Kim, in *Supported Catalysts and Their Applications*, ed. D. C. Sherrington and A. P. Kybett, The Royal Society of Chemistry, 2001, pp. 19–26, DOI: 10.1039/9781847551962-00019.

34 K. Sing, D. Everett, R. Haul, L. Moscou, R. Pierotti, J. Rouquerol and T. Siemieniewska, *Pure Appl. Chem.*, 1985, **57**, 603–619.

35 R. Jin, Z. Wu, Y. Liu, B. Jiang and H. Wang, *J. Hazard. Mater.*, 2009, **161**, 42–48.

36 A. Sorrentino, S. Rega, D. Sannino, A. Magliano, P. Ciambelli and E. Santacesaria, *Appl. Catal., A*, 2001, **209**, 45–57.

37 M. Kobayashi and M. Hagi, *Appl. Catal., B*, 2006, **63**, 104–113.

38 S. Liu, E. Guo and L. Yin, *J. Mater. Chem.*, 2012, **22**, 5031–5041.

39 J. P. Chen and R. T. Yang, *J. Catal.*, 1993, **139**, 277–288.

40 J. Y. Cho, W. H. Nam, Y. S. Lim, W.-S. Seo, H.-H. Park and J. Y. Lee, *RSC Adv.*, 2012, **2**, 2449–2453.

41 C. Marinescu, A. Sofronia, C. Rusti, R. Piticescu, V. Badilita, E. Vasile, R. Baies and S. Tanasescu, *J. Therm. Anal. Calorim.*, 2011, **103**, 49–57.

42 D. A. H. Hanaor and C. C. Sorrell, *J. Mater. Sci.*, 2011, **46**, 855–874.

43 R. Rejeb, L. Khalfallah Boudali, G. Delahay and C. Petitto, *Top. Catal.*, 2016, 1–8.

44 A. Rajaeiyan and M. M. Bagheri-Mohagheghi, *Adv. Manuf.*, 2013, **1**, 176–182.

45 C. Ren, W. Qiu and Y. Chen, *Sep. Purif. Technol.*, 2013, **107**, 264–272.

46 C. Orsenigo, L. Lietti, E. Tronconi, P. Forzatti and F. Bregani, *Ind. Eng. Chem. Res.*, 1998, **37**, 2350–2359.

47 R. Camposeco, S. Castillo and I. Mejía-Centeno, *Catal. Commun.*, 2015, **60**, 114–119.

48 L. Ma, J. Li, R. Ke and L. Fu, *J. Phys. Chem. C*, 2011, **115**, 7603–7612.

49 S. T. Choo, Y. G. Lee, I.-S. Nam, S.-W. Ham and J.-B. Lee, *Appl. Catal., A*, 2000, **200**, 177–188.

50 S. M. Jung and P. Grange, *Appl. Catal., B*, 2001, **32**, 123–131.

51 J. P. Chen and R. T. Yang, *J. Catal.*, 1990, **125**, 411–420.

52 F. Liu, Y. Yu and H. He, *Chem. Commun.*, 2014, **50**, 8445–8463.

53 L. Zhang, L. Shi, L. Huang, J. Zhang, R. Gao and D. Zhang, *ACS Catal.*, 2014, **4**, 1753–1763.

54 T. Mishra and K. M. Parida, *J. Colloid Interface Sci.*, 2006, **301**, 554–559.

55 M. Casanova, L. Nodari, A. Sagar, K. Schermanz and A. Trovarelli, *Appl. Catal., B*, 2015, **176–177**, 699–708.

56 H. Hu, S. Cai, H. Li, L. Huang, L. Shi and D. Zhang, *ACS Catal.*, 2015, **5**, 6069–6077.

57 Z. Fan, H. Guo, K. Fang and Y. Sun, *RSC Adv.*, 2015, **5**, 24795–24802.

58 S. Matsuda, T. Kamo, A. Kato, F. Nakajima, T. Kumura and H. Kuroda, *Ind. Eng. Chem. Prod. Res. Dev.*, 1982, **21**, 48–52.